NANO LETTERS

pubs.acs.org/NanoLett

Letter

Near-Field Radiative Heat Transfer Modulation with an Ultrahigh Dynamic Range through Mode Mismatching

Kezhang Shi, Zhaoyang Chen, Yuxin Xing, Jianxin Yang, Xinan Xu, Julian S. Evans, and Sailing He*

Cite This: *Nano Lett.* 2022, 22, 7753−7760

Read Online

ACCESS | Metrics & More | Article Recommendations | Supporting Information

ABSTRACT: Modulating near-field radiative heat transfer (NFRHT) with a high dynamic range is challenging in nanoscale thermal science and engineering. Modulation depths [(maximum value − minimum value)/(maximum value + minimum value) × 100%] of ≈2% to ≈15.7% have been reported with matched modes, but breaking the constraint of mode matching theoretically allows for higher modulation depth. We demonstrate a modulation depth of ≈32.2% by a pair of graphene-covered SU8 heterostructures at a gap distance of ≈80 nm. Dissimilar Fermi levels tuned by bias voltages enable mismatched surface plasmon polaritons which improves the modulation. The modulation depth when switching from a matched mode to a mismatched mode is ≈4.4-fold compared to that when switching between matched modes. This work shows the importance of symmetry in polariton-mediated NFRHT and represents the largest modulation depth to date in a two-body system with fixed gap distance and temperature.

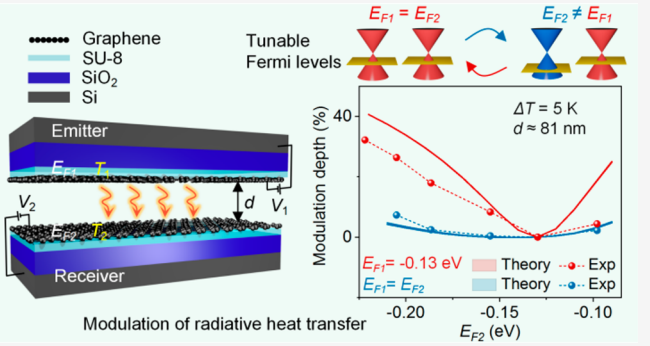

KEYWORDS: *modulation of near-field radiative heat transfer, graphene, surface plasmon polaritons coupling, mode mismatching, fluctuational electrodynamics, radiative heat transfer measurement*

Thermal radiation, with spectral and power density properties described by Planck's Law and the Stefan−Boltzmann Law, is one of the known noncontact heat transfer modes in vacuum.[1,2] Classical physics predicts that a perfect thermal emitter operates at the blackbody (BB) limit. Fluctuational electrodynamics has demonstrated that evanescent modes, including plasmon and phonon polaritons, allow large near-field radiative heat transfer (NFRHT) far beyond the limit.[3−14] Compared to the general far-field broadband radiative spectrum, NFRHT is primarily dominated by the resonance coupling modes between two close objects, allowing for active control of the spectrum[11,15] and energy transfer.[6,16]

Dynamic modulation of NFRHT requires changing the optical responses of the emitter and receiver to modulate the radiative heat flux. Previous works[17−20] have shown that a phase-change material (VO_2) allows for thermal radiation modulation due to its insulator-to-metal transition. However, the modulation requires temperature variation. Graphene has highly tunable surface plasmon polaritons (SPPs) related to its Fermi level in a linear Dirac band, which makes it an ideal thermal modulator with external stimuli at a fixed operating temperature.[21−23] Altering the free carrier states of a van der Waals' heterostructure also allows for exotic nanoscale phenomena such as tunable Mott insulator,[24] nanoimaging in an infrared-waveguide,[25] and efficient Fizeau drag from Dirac electrons,[26] etc. Recent experimental works have demonstrated that graphene plasmons enable giant radiative heat transfer at the nanoscale.[5,6,12] Graphene with different Fermi levels supports tunable SPPs and accounts for different radiative heat flux. A high dynamic range modulation of NFRHT allows for a high signal-to-noise ratio (SNR) enabling potential applications in thermal switches and communication. Thomas et al. have shown an electronic modulation depth of ≈2% [defined by (maximum value−minimum value)/(maximum value + minimum value) × 100%] with a pair of graphene sheets on Al_2O_3/SiO_2 substrate.[21] The Fermi levels of the two graphene sheets are assumed to be equal since the samples are in conductive contact. Our recent work has shown that the modulation depth could reach ≈15.7% with stacked graphene layers at similar Fermi levels.[6] However, the modulation effect is limited by the matched resonance modes between the identical graphene sheets, as the graphene on the emitter and receiver have similar Fermi levels.

Here, we present a significant modulation improvement by a pair of graphene/SU8 heterostructures at a gap distance of ≈80 nm. Back-gated tuning was employed for the graphene

Received: March 31, 2022
Revised: September 21, 2022
Published: September 26, 2022

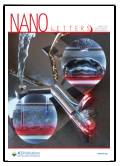

https://doi.org/10.1021/acs.nanolett.2c01286
Nano Lett. 2022, 22, 7753−7760

Fermi level control. The mismatched SPPs due to different Fermi levels of the two graphene sheets allow for a much smaller heat flux compared to the matched SPPs case. The measured maximum modulation depth could reach ≈32.2% and is ≈4.4-fold compared to that of the matched case. This experimental work represents the largest modulation depth ever reported for the radiative heat transfer in a two-body planar system with a fixed gap distance and operating temperature. The mode-mismatch-induced high-efficiency NFRHT modulation should inspire potential applications of thermal switches,[22,27,28] thermal communication, and is suitable for tunable plasmon- or phonon-induced thermal or photonic regulation.

We study the NFRHT between a pair of graphene-covered SU8 heterostructures on SiO_2/Si substrates (marked as Gr/SU8, Figure 1). The thickness of the SU8 is chosen to be 90 nm to reduce the influence of phonon polaritons from the substrate. Based on the fluctuational electrodynamics, the net radiative heat flux between the emitter and receiver (with temperatures T_1 and T_2, respectively) at a gap distance d is calculated by[29−33]

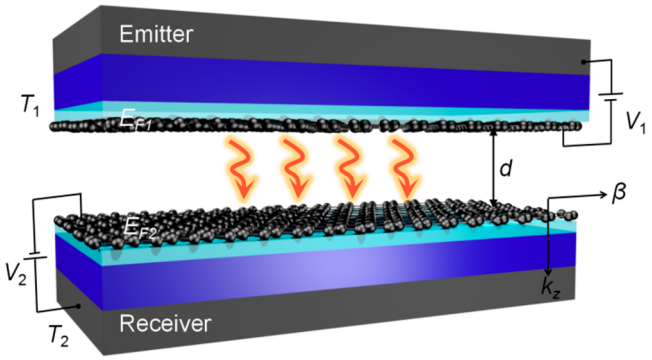

Figure 1. Schematic illustration of a pair of graphene-covered SU8 heterostructures (on SiO_2/Si substrates) separated by a vacuum gap distance d. T_1 and T_2 are set to 308.15 and 303.15 K, respectively. A back-gated tuning method with applied bias voltages V_1 and V_2 is employed to control the Fermi levels of the two graphene sheets. The red arrows illustrate the net radiative heat flux flowing from the emitter to the receiver.

$$Q = \frac{1}{4\pi^2}\int_0^\infty \left\{ [\Theta(T_1,\omega) - \Theta(T_2,\omega)] \times \left[\int_0^{k_0} \beta \sum_{j=s,p} \xi_j(\omega,\beta,d)\mathrm{d}\beta + \int_{k_0}^\infty \beta \sum_{j=s,p} \xi_j(\omega,\beta,d) \times d\beta \right] \right\} \mathrm{d}\omega \quad (1)$$

where $\Theta(T,\omega) = \hbar\omega/[\exp(\hbar\omega/k_BT) - 1]$ is the mean energy of the Planck thermal harmonic oscillators without zero point energy. $\hbar$ is the reduced Planck constant and k_B is the Boltzmann constant. ξ_j represents the energy transmission coefficient between the emitter and receiver (considering both s- and p-polarization modes):

$$\xi_j(\omega,\beta) = \begin{cases} \dfrac{(1-|r_{j,e}|^2)(1-|r_{j,r}|^2)}{|1 - r_{j,e}r_{j,r}e^{2ik_{z0}d}|^2}, & \beta < k_0 \\ \dfrac{4\mathrm{Im}(r_{j,e})\mathrm{Im}(r_{j,r})e^{2ik_{z0}d}}{|1 - r_{j,e}r_{j,r}e^{2ik_{z0}d}|^2}, & \beta > k_0 \end{cases} \quad (2)$$

where k_{z0} is the z-component of the wave vector in vacuum (k_0). $r_{j,e}$ and $r_{j,r}$ are the Fresnel reflection coefficients of the emitter and receiver, respectively. ξ_p with $\beta > k_0$ represents the photon tunneling probability of the p-polarized evanescent modes.

For a homogeneous medium with finite thickness, the reflection coefficients become[29,32]

$$r_j = \begin{cases} \dfrac{r_{s01} + r_{s12}(1 + r_{s01} + r_{s10})e^{2ik_z^{(1s)}h_1}}{1 - r_{s10}r_{s12}e^{2ik_z^{(1s)}h_1}}, & j = s \\ \dfrac{r_{p01} + r_{p12}(1 - r_{p01} - r_{p10})e^{2ik_z^{(1p)}h_1}}{1 - r_{p10}r_{p12}e^{2ik_z^{(1p)}h_1}}, & j = p \end{cases} \quad (3)$$

where h_1 is the thickness of layer one and $r_{s(p),01}$ is the Fresnel reflection coefficient at the interface between layer 0 and layer 1 for s- or p-polarization modes:

$$r_{j01} = \begin{cases} \dfrac{k_z^{(0s)} - k_z^{(1s)} - \sigma\mu_0\omega}{k_z^{(0s)} + k_z^{(1s)} + \sigma\mu_0\omega}, & j = s \\ \dfrac{k_z^{(0p)}\varepsilon_\perp^{(1)} - k_z^{(1p)}\varepsilon_\perp^{(0)} + \frac{\sigma k_z^{(0p)}k_z^{(1p)}}{\varepsilon_0\omega}}{k_z^{(0p)}\varepsilon_\perp^{(1)} + k_z^{(1p)}\varepsilon_\perp^{(0)} + \frac{\sigma k_z^{(0p)}k_z^{(1p)}}{\varepsilon_0\omega}}, & j = p \end{cases} \quad (4)$$

where $k_z^{(np)} = \left(\varepsilon_\perp^{(n)}k_0^2 - \frac{\varepsilon_\perp^{(n)}}{\varepsilon_\parallel^{(n)}}\beta^2\right)^{1/2}$, $k_z^{(ns)} = (\varepsilon_\perp^n k_0^2 - \beta^2)^{1/2}$, n = 0, 1, 2 is the number of the layers, $\varepsilon_\perp^{(n)}$ and $\varepsilon_\parallel^{(n)}$ are the perpendicular and parallel components of the relative dielectric tensor. Here, $\varepsilon_\perp^{(n)} = \varepsilon_\parallel^{(n)}$ is set for the isotropic medium. Graphene was treated as surface current with complex conductivity σ:[34,35]

$$\sigma = \frac{2ie^2k_BT\ \ln[2\cosh[E_F/(2k_BT)]]}{(\omega + i/\tau)\pi\hbar^2} + \frac{e^2}{4\hbar}\left[G\left(\frac{\hbar\omega}{2}\right) + \frac{i4\hbar\omega}{\pi}I\right] \quad (5)$$

where

$$I = \int_0^\infty \left[G(\delta) - G\left(\frac{\hbar\omega}{2}\right)\right]/[(\hbar\omega)^2 - 4\delta^2]\mathrm{d}\delta \quad (6)$$

$$G(\delta) = \sinh(\delta/k_BT)/[\cosh(E_F/k_BT) + \cosh(\delta/k_BT)] \quad (7)$$

The left and right terms in eq 5 account for the intraband and interband electron transitions, respectively. E_F is the Fermi level of graphene. τ = 100 fs related to the carrier−carrier intraband collisions and phonon emission is used in our calculations for the collision time.[5,6,12,36,37] The dielectric function of the vacuum-like SU8 material was modeled as multiple Lorentz−Drude oscillators,[6,38] while the dielectric

https://doi.org/10.1021/acs.nanolett.2c01286
Nano Lett. 2022, 22, 7753−7760

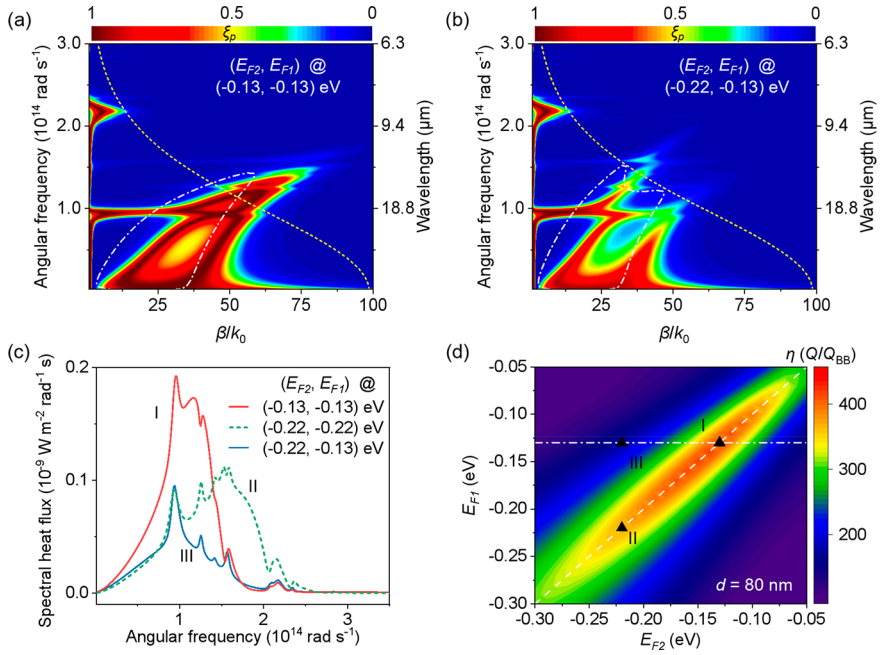

Figure 2. Calculation and analysis of the NFRHT modulation of Gr/SU8 heterostructures at d = 80 nm with T_1 = 308.15 K and T_2 = 303.15 K. Contour maps of ξ_p for a pair of Gr/SU8 heterostructures (on SiO_2/Si substrates) with $E_{F2} = E_{F1} = -0.13$ eV for (a) and $E_{F2} = -0.22$ eV, $E_{F1} = -0.13$ eV for (b). The yellow-dashed lines in (a) and (b) correspond to the occupation factor $\Theta(T_1,\omega) - \Theta(T_2,\omega)$ in arbitrary units, while dashed-dotted lines are the dispersion curves of the coupled SPPs of the two suspended graphene sheets. (c) Spectral heat flux of Gr/SU8 heterostructures for three cases of graphene Fermi levels (E_{F2}, E_{F1}), where $E_{F2} = E_{F1} = -0.13$ eV for case I (red-solid line), $E_{F2} = E_{F1} = -0.22$ eV for case II (green-dotted line), and $E_{F2} = -0.22$ eV, $E_{F1} = -0.13$ eV for the mismatched case III (blue-solid line). (d) Contour map of the radiative heat flux Q normalized with the corresponding BB limit with E_{F2} and E_{F1} ranging from −0.3 eV to −0.05 eV. The white-dashed-dotted line corresponds to the cases of mismatched resonance modes, while the white-dashed line (along the diagonal direction) represents the cases of the matched SPPs.

function of SiO_2 was taken from ref 39. The Si substrate was omitted due to its negligible contribution to the NFRHT.

The photon tunneling probability ξ_p of the evanescent modes between the emitter and receiver at a gap distance of 80 nm is calculated and shown in Figure 2a,b. Strong coupling modes arising from the matched SPPs could be observed when the graphene Fermi levels of the receiver (E_{F2}) and emitter (E_{F1}) are both −0.13 eV (Figure 2a), corresponding to our experiment with bias voltages (V_2, V_1) = (35, 35) V. The SPP coupling modes are slightly deviated from the ideal dispersion curves of a pair of suspended graphene sheets (dashed-dotted lines) due to the impact of the SU8 spacers and the SiO_2 substrates. Typical phonon polaritons from the SiO_2 substrate support the near-unity ξ_p around wavelengths of 8.56 and 19.9 μm, but have no contribution to the heat flux modulation. The yellow-dashed lines correspond to the occupation factor $\Theta(T_1,\omega) - \Theta(T_2,\omega)$ in arbitrary units. The near-unity ξ_p overlaps the dispersion curves of the SPP coupling modes of two Gr/SU8 heterostructures (not shown). The coupled modes split into two branches at a lower β but merge at a larger β, as the larger loss (at large β) in the vertical direction enables rapid attenuation of the SPP modes and prevents the interaction between the emitter and receiver. These matched SPP coupling modes are supported at the mid- and far-infrared regions with a larger occupation factor and are the dominant contributor to the radiative heat flux. Compared with changing the graphene Fermi levels synchronously (e.g., change both E_{F2} and E_{F1} to −0.22 eV), producing dissimilar Fermi levels is a more effective way to pursue an improved modulation depth. When only the graphene Fermi level of the receiver changes to −0.22 eV (Figure 2b), the SPPs arising from the emitter and receiver contribute less to the near-unity ξ_p. Due to the mismatched SPP modes, the resonance modes are decoupled around 1.0×10^{14} and 1.5×10^{14} rad/s with large β. In contrast, the phonon polaritons modes remain unchanged due to the identical SiO_2 substrates on both sides. The spectral heat flux (after integration over β) between the Gr/SU8 heterostructures shows the influence of the graphene SPPs with identical or dissimilar Fermi levels (Figure 2c). When $E_{F2} = E_{F1} = -0.13$ eV (case I), the spectrum attributed to the matched strong SPPs covers a broad frequency region with the highest value. A broader spectrum with lower spectral heat flux (compared to case I) could be observed when $E_{F2} = E_{F1} = -0.22$ eV (case II). However, the spectral heat flux decreases dramatically when E_{F2} is not equal to E_{F1}, where $E_{F2} = -0.22$ and $E_{F1} = -0.13$ eV (case III). The spectrum in case III shares a similar frequency region with case I, but it has smaller intensity due to the mismatched resonance modes. The radiative heat flux reaches 1.34×10^4, 1.19×10^4, and 0.57×10^4 W/m^2 for cases I, II, and III, respectively. This leads to a remarkable improvement of the NFRHT modulation depth from case I to case III, where the modulation depth is 40.3% [calculated by (radiative heat flux of case I − radiative heat flux of case III)/(radiative heat flux of case I + radiative heat flux of case III) × 100%] and is ≈6.7-fold compared to that from case I to case II. Figure 2d gives the contour map of the radiative heat flux normalized with corresponding BB limit with variable E_{F1} and E_{F2}. For different E_{F1} at a fixed E_{F2}, the radiative heat flux arrives at a maximal value with two similar E_F. This confirms the importance of the symmetry of the polariton-mediated NFRHT system. White-dashed line shows the cases with matched coupling SPP modes. Case I with η = 416 is quite close to the peak point at $E_{F2} = E_{F1} = -0.14$ eV. The white-dashed-dotted line highlights the cases corresponding to

https://doi.org/10.1021/acs.nanolett.2c01286
Nano Lett. 2022, 22, 7753−7760

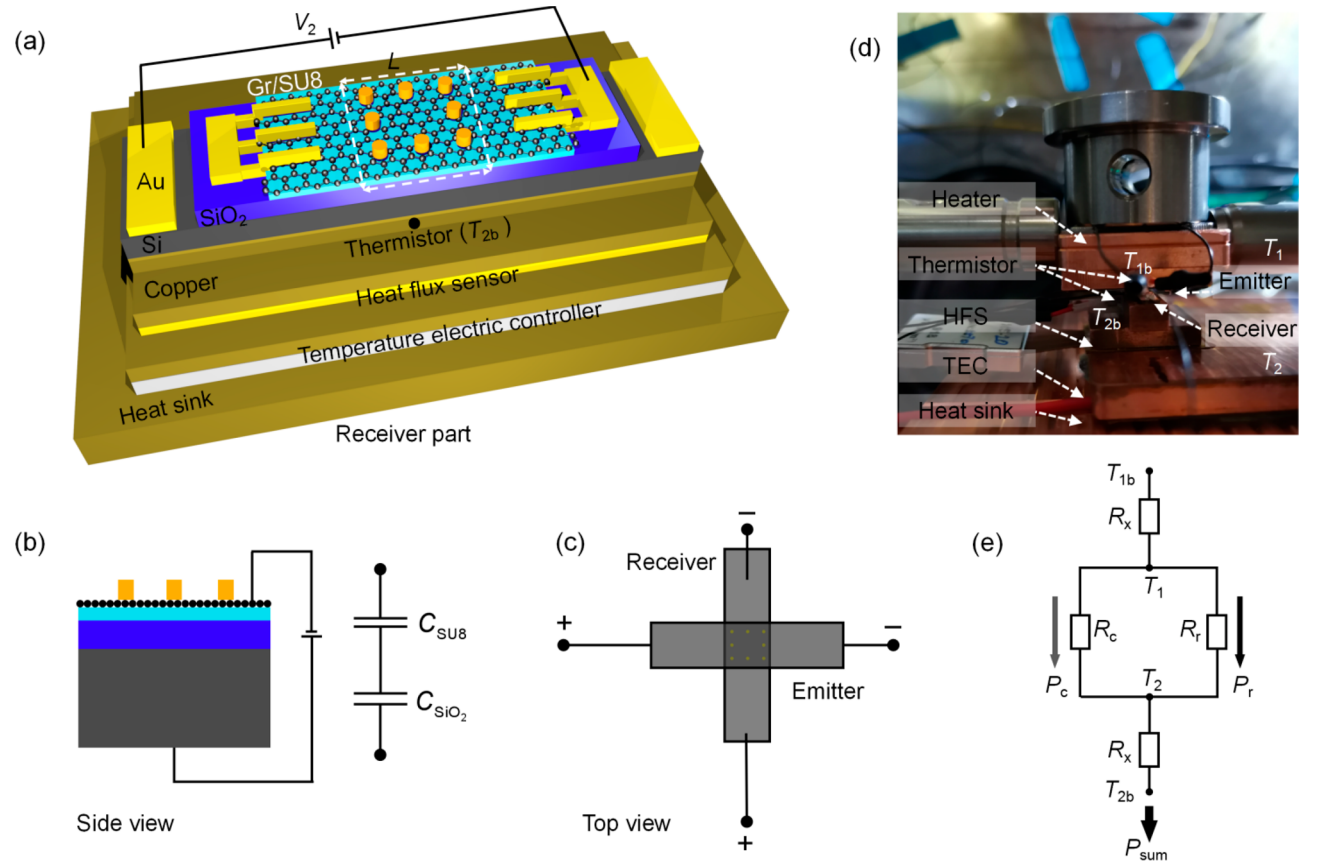

Figure 3. Schematic illustrations of the NFRHT experimental setup. (a) Schematic diagram of the receiver part. White-dashed square shows the active area of 3 × 3 mm^2. Au/Ti electrodes for both emitter and receiver are conductively contacted with the graphene sheets to control the Fermi level by the external electrostatic field. (b) Side view of the receiver. The receiver (or emitter) was modeled as two capacitors in series, where C_{su8} and C_{SiO_2} are the capacitances per unit area of the SU8 spacer and SiO_2 dielectric, respectively. The graphene Fermi level was determined by the equivalent capacitance model. (c) Top view of the emitter and receiver. The conductive wires with positive and negative signs correspond to the two independent back-gated devices. (d) Photo of the NFRHT experimental device in a vacuum chamber. The heater and temperature electric controller (TEC) were used to control the temperature of the emitter and receiver, respectively. The embedded thermistors were used to measure the backside temperature T_{2b} (T_{1b}) of the receiver (emitter). See more discussion in SI section 3. (e) Equivalent thermal circuit of the NFRHT experimental device. P_{sum} is the sum of the heat powers contributed by the heat conduction portion (P_c) and the radiative portion (P_r). R_c and R_r are the thermal conduction resistance and equivalent thermal radiation resistance, respectively. T_1 and T_2 are the top surface temperatures of the emitter and receiver, respectively, estimated by the measured sum R_x (SI section 3) of the thermal resistances of the sample, thermal conductive adhesive, and the copper carrier. T_2 was maintained at 303.15 K, while T_1 was 308.15 K unless otherwise specified.

the mismatched resonance modes. Finding a point with smaller heat flux based on the mismatched graphene Fermi levels allows for a higher modulation depth. In this work, the radiative heat flux from case I to case II, and case I to case III were measured.

The emitter and receiver consist of single-layer graphene-covered SU8 heterostructures on the 300 nm-thick SiO_2 on Si substrates (see Supporting Information (SI) section 2). Eight identical SU8 nanopillars with thickness of ≈90 nm were fabricated on the surface of the graphene sheets for the receiver (Figure 3a). A back-gated device was employed to tune the Fermi levels of graphene. Figure 3b shows the side view of the receiver within the active area (white-dashed square with L = 3 mm in Figure 3a). A positive (negative) $V_g - V_n$ induces electron (hole) doping,[40,41] allowing an excess-electron surface concentration of $n = \eta_c(V_g - V_n)$, where V_g is the gate-tuning voltage, V_n is the voltage at the charge neutral point, and η_c is a coefficient related to the back-gated structure with gate insulators composed of 90 nm thick SU8 and 300 nm thick SiO_2 (see SI section 1). The graphene Fermi levels could be obtained by $E_F = \mathrm{sgn}(n)\ \hbar V_F(\pi\ |n|)^{1/2}/e$ (unit: eV), where $\mathrm{sgn}(x)$ is the sign of x and $V_F = 1 \times 10^6$ m/s is the Fermi velocity of graphene.[40−44] The emitter was pressed on the receiver in a cross shape and separated by the SU8 nanopillars (Figure 3c). A total of 95 g mass above the emitter and two fixed posts were used to strengthen the contact and mechanical stability of the system (Figure 3d).[6,10,12,33] The gap distance was estimated within a range from ≈79 to ≈83 nm (i.e., at an average value of ≈81 nm) based on the one-dimensional linear elastic analysis[6] (SI section 4). Figure 3e illustrates the equivalent thermal circuit of the system. P_{sum} detected by the heat flux sensor (HFS) is the sum heat power of P_c and P_r, where P_r is the near-field radiative heat power including the contribution of both propagating waves and evanescent waves. The measured radiative heat flux could be obtained by $Q = (P_{sum} - P_c)/A$, where A is the active area of 3 × 3 mm^2. P_c is the heat conduction from the eight SU8 nanopillars and is calculated based on Fourier's Law (SI section 5).

The radiative heat flux shown in Figure 4a was measured at T_2 = 303.15 K with temperature difference ΔT of 5 K at a gap distance of ≈81 nm. When no bias voltages are applied to the emitter and receiver, i.e., $(V_2, V_1) = (0, 0)$ V, E_{F2} and E_{F1} are

https://doi.org/10.1021/acs.nanolett.2c01286
Nano Lett. 2022, 22, 7753−7760

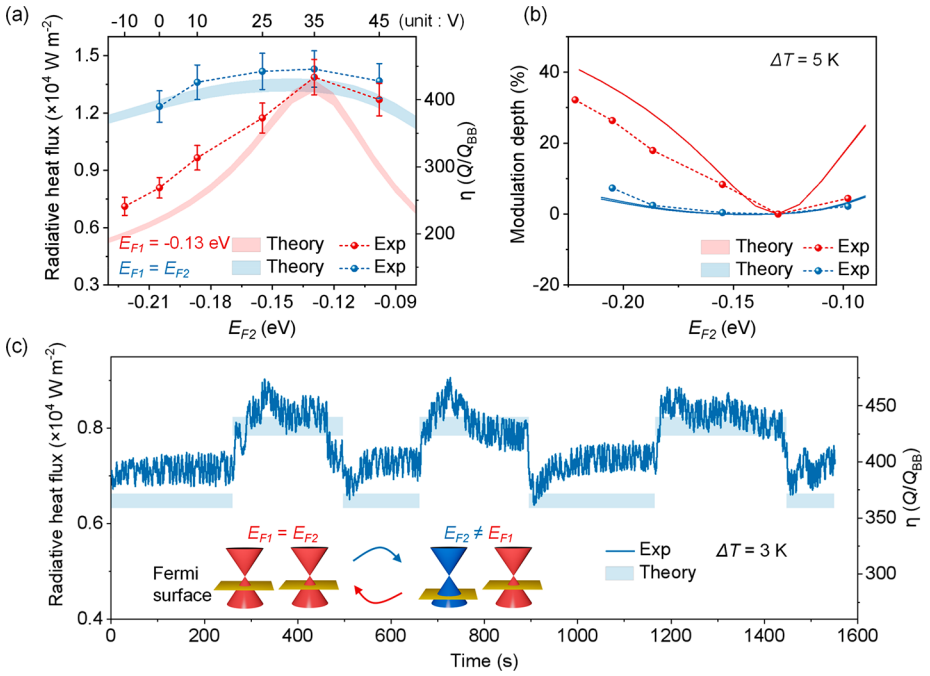

Figure 4. Measurements and analysis of the NFRHT modulation of the Gr/SU8 heterostructures at the gap distance of ≈81 nm with different bias voltages. The colored bands in all panels are the corresponding theoretical calculation with d from 79 to 81 nm. (a) Radiative heat flux varies with the bias voltages (graphene Fermi levels) at temperature difference ΔT = 5 K for the matched cases (blue lines) and the mismatched cases (red lines). Each point of the curves in (a) and (b) is an average value from three possible active areas (2.9 × 2.9 mm^2, 3 × 3 mm^2, and 3.1 × 3.1 mm^2) after measuring for four times from the external heat flux meter. Error bars were plotted due to the uncertainty of the active area (see SI section 6). (b) Modulation depth of different graphene Fermi levels corresponding to the matched and mismatched cases in (a). The modulation depth is calculated by (measured maximum value−other measured value)/(measured maximum value + other measured value) × 100%. (c) Time-varying heat flux of the Gr/SU8 heterostructures at ΔT = 3 K. Blue-solid line is the measured radiative heat flux and the blue bands are the theoretical prediction. Inset shows the illustrations of the tunable graphene Fermi levels of the emitter and receiver due to different applied bias voltages.

calculated to be −0.205 eV according to the measured radiative heat flux. According to the back-gated method, other bias voltages of (10, 10), (25, 25), (35, 35), and (45, 45) V correspond to the graphene Fermi levels of −0.187, −0.155, −0.13, and −0.098 eV respectively. The Fermi levels become closer to the Dirac point with higher positive voltages, indicating the hole doping of the graphene sheets. When E_{F2} = E_{F1} = −0.13 eV, the matched SPPs allow for the broadband near-unity ξ_p within the desired mid- and far-infrared region, producing the best performance among all measured cases. The radiative heat flux reaches 1.43 × 10^4 W/m^2 and is ≈441-fold of the corresponding BB limit. When E_{F2} = E_{F1} = −0.205 eV, the enhancement (≈ 381-fold with respect to the BB limit) is relatively robust, as the SPP modes of the emitter and receiver are still matched, despite the blue-shift to a higher frequency region with less occupation factor (similar to the spectral heat flux of case II in Figure 2c). For the mismatched cases, the bias voltage of the emitter V_1 is fixed at 35 V while the bias voltage of the receiver V_2 is set to −10, 0, 10, 25, 35, and 45 V. Remarkable modulation of the radiative heat flux was observed when the bias voltage of the receiver became different from that of the emitter. Here the minimum radiative heat flux (≈ 220-fold with respect to the BB limit) was observed at (V_2, V_1) = (−10, 35) V, where the graphene Fermi levels are dissimilar [i.e., (E_{F2}, E_{F1}) = (−0.22, −0.13) eV]. When V_2 increases to 35 V again, the radiative heat flux can still reach a peak value of 1.39 × 10^4 W/m^2 with enhancement of ≈429-fold of the BB limit, indicating the robustness of the tuning devices. Figure 4b illustrates the modulation depths [(measured maximum value−other measured value)/(measured maximum value + other measured value) × 100%] of the matched and mismatched cases, respectively. The maximum modulation depth achievable with only matched cases is ≈7.3% going from (E_{F2}, E_{F1}) = (−0.13, −0.13) eV to (E_{F2}, E_{F1}) = (−0.205, −0.205) eV, but the modulation depth is ≈26.3% when only changing E_{F2} to −0.205 eV. The maximum modulation depth from the matched case to a mismatched case reaches ≈32.2% when tuning E_{F2} to −0.22 eV by applying −10 V bias voltage to the receiver. It could potentially be further improved when other larger negative voltages are applied. Considering the breakdown of the capacitor-like samples, only −10 V was investigated in this work. Construction of the mismatched resonance modes plays a significant role in the NFRHT modulation improvement. Switching the symmetry of the polariton-mediated near-field system gives promising high-efficiency modulation in thermal radiation. The modulation depth of ≈32.2% is ≈4.4-fold compared to that for the matched cases and is 16.1-fold of the previous report on graphene-based heterostructures.[21] The modulation of the radiative heat flux at another ΔT of 3 K was also investigated in Figure 4c. The time-varying heat flux were recorded by the HFS when changing the bias voltages from (V_2, V_1) = (35, 35) V to (25, 35) V repeatedly. The average modulation depth of ≈7% is similar to that with ΔT = 5 K in Figure 4b (≈ 8.3%). Small ΔT (like that in this work) is more likely required in potential applications such as thermal communication, since the state of the thermal equilibrium will be easier to achieve after switching the graphene Fermi levels, hence a faster response time. The results show good repeatability and robustness of our devices for the NFRHT

https://doi.org/10.1021/acs.nanolett.2c01286
Nano Lett. 2022, 22, 7753−7760

modulation. The sample in this work consists of a single-layer graphene-covered SU8 heterostructure, which is simpler and easier to fabricate, and allows for larger modulation depth (with mismatched modes) than that of the previous work[6] with multilayer structure (only matched modes are considered). The physical mechanism in ref 6. is that multilayer systems allow many branches in k-space to provide stronger NFRHT and modulation with the tuning of only one Fermi level was used for the optimal radiative heat flux. This work focused on the ultrahigh dynamic modulation and the essential physics is that independent tuning of two different Fermi levels allows a massive improvement in modulation depth. In addition, the determination of the graphene Fermi level is significantly improved by the equivalent capacitance model related to the back-gated tuning devices.

The modulation depth versus variable vacuum gap distance d within a range from 50 to 500 nm is theoretically investigated (Figure 5). The black-dashed line shows the gap-dependent

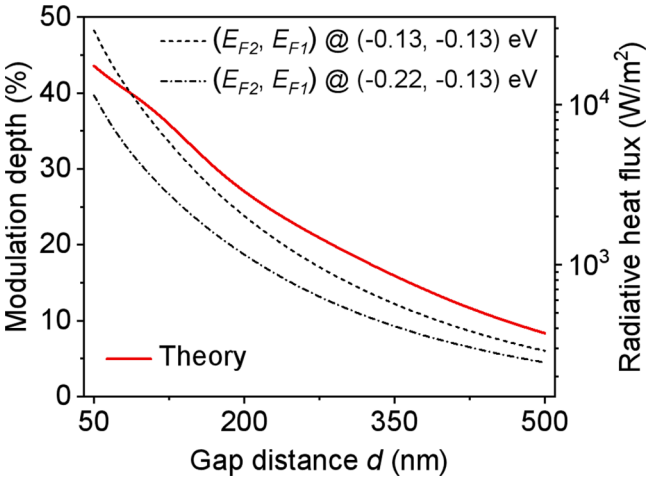

Figure 5. Calculated modulation depth (red-solid line) versus variable vacuum gap distance d within a range from 50 to 500 nm. The temperatures of the emitter and receiver are set to 308.15 and 303.15 K, respectively. The black-dashed line and dashed-dotted line show the calculated radiative heat flux between two Gr/SU8 heterostructures with graphene Fermi levels of (E_{F2}, E_{F1}) = (−0.13, −0.13) eV and (E_{F2}, E_{F1}) = (−0.22, −0.13) eV, respectively.

radiative heat flux between two identical Gr/SU8 heterostructures with (E_{F2}, E_{F1}) = (−0.13, −0.13) eV, and the dashed-dotted line indicates the mismatched cases with (E_{F2}, E_{F1}) = (−0.22, −0.13) eV. The modulation depths (red-solid line) are calculated by the radiative heat flux when switching the graphene Fermi levels from (−0.13, −0.13) eV to (−0.22, −0.13) eV at the corresponding d. The modulation depth can be improved to 43.6% at d = 50 nm. The modulation depth decreases as d increases and could still reach 8.4% when d = 500 nm. In general, the modulation effect of the NFRHT is stronger with smaller gap distances due to the near-field effect of the graphene plasmon polaritons.

In conclusion, we have experimentally demonstrated an improved radiative heat flux control with an ultrahigh modulation depth of ≈32.2% with a pair of graphene-covered SU8 heterostructures at a gap distance of ≈80 nm. Tuning the graphene Fermi levels allows for coupling or decoupling of the SPP modes. Breaking the symmetry of the SPP resonance modes by changing the Fermi level of either the emitter or the receiver provides a much higher NFRHT modulation depth compared to other known methods. The theoretical analysis of the gap-dependence of the modulation depth shows that the modulation effect of the NFRHT is stronger with smaller gap distances due to the near-field effect of the graphene plasmon polaritons. This work focused on the dynamic modulation of the NFRHT by the mode mismatching method and is important for the fundamental understanding of the tunable collective optoelectronic phenomena for light−matter interaction and heat transfer at the nanoscale. The method is feasible for other van der Waals' heterostructures with resonance modes sensitive to external stimuli. The experimental results obtained in this work provide strong evidence on mode-mismatch-induced ultrahigh dynamic NFRHT modulation with polariton-mediated materials in the near-field systems, which is of fundamental interest in polaritons control and energy manipulation. This result should inspire potential applications such as thermal switches and thermal communication.

■ ASSOCIATED CONTENT

Supporting Information

The Supporting Information is available free of charge at https://pubs.acs.org/doi/10.1021/acs.nanolett.2c01286.

Back-gated tuning of the graphene Fermi level; sample fabrication and characterization; experimental setup and measurement of the thermal resistance R_x; gap distance between the emitter and receiver; heat conduction of the SU8 nanopillars; uncertainty analysis of the measured radiative heat flux (PDF)

■ AUTHOR INFORMATION

Corresponding Author

Sailing He − *Centre for Optical and Electromagnetic Research, National Engineering Research Center for Optical Instruments, Zhejiang University, Hangzhou 310058, China; Shanghai Institute for Advanced Study, Zhejiang University, Shanghai 201203, China; Department of Electromagnetic Engineering, School of Electrical Engineering, Royal Institute of Technology, Stockholm S-100 44, Sweden;* orcid.org/0000-0002-3401-1125; Email: sailing@kth.se

Authors

Kezhang Shi − *Centre for Optical and Electromagnetic Research, National Engineering Research Center for Optical Instruments, Zhejiang University, Hangzhou 310058, China;* orcid.org/0000-0002-9861-3213

Zhaoyang Chen − *Centre for Optical and Electromagnetic Research, ZJU-SCNU Joint Center of Photonics, South China Academy of Advanced Optoelectronics, South China Normal University, Guangzhou 510006, China*

Yuxin Xing − *Centre for Optical and Electromagnetic Research, National Engineering Research Center for Optical Instruments, Zhejiang University, Hangzhou 310058, China; Shanghai Institute for Advanced Study, Zhejiang University, Shanghai 201203, China*

Jianxin Yang − *Centre for Optical and Electromagnetic Research, ZJU-SCNU Joint Center of Photonics, South China Academy of Advanced Optoelectronics, South China Normal University, Guangzhou 510006, China*

https://doi.org/10.1021/acs.nanolett.2c01286
Nano Lett. 2022, 22, 7753−7760

Xinan Xu − *Centre for Optical and Electromagnetic Research, National Engineering Research Center for Optical Instruments, Zhejiang University, Hangzhou 310058, China*

Julian S. Evans − *Centre for Optical and Electromagnetic Research, National Engineering Research Center for Optical Instruments, Zhejiang University, Hangzhou 310058, China;* orcid.org/0000-0003-4937-0582

Complete contact information is available at: https://pubs.acs.org/10.1021/acs.nanolett.2c01286

Author Contributions

S.H. conceived and supervised the work. K.S. conceived the work and performed the calculations. K.S., Z.C., J.Y., and X.X. fabricated the samples. K.S., Z.C., and J.Y. performed the sample characterization. K.S. and Z.C. performed the experiments. The manuscript was discussed and written by K.S., J.E., Y.X., and S.H. with comments and input from all authors.

Notes

The authors declare no competing financial interest.

■ ACKNOWLEDGMENTS

This work was partially supported by the National Natural Science Foundation of China (No. 91233208, 91833303, 11621101, 61550110246), the National Key Research and Development Program of China (No. 2017YFA0205700, 2018YFC1407503), Special Development Fund of Shanghai Zhangjiang Science City, Key Research and Development Program of Zhejiang Province (2021C03178) and Guangdong Innovative Research Team Program (No. 201001D0104799318) and China Postdoctoral Science Foundation (2022M710122). The authors also appreciate the discussions with Dr. Xiaobo Xing from South China Normal University and Dr. Xiaohu Wu from Shandong Institute of Advanced Technology.

■ REFERENCES

(1) Planck, M. *The Theory of Heat Radiation* [transl. Masius, M.]; P. Blakiston's Son & Co.: Philadelphia, 1914.

(2) Fong, K. Y.; Li, H. K.; Zhao, R.; Yang, S.; Wang, Y.; Zhang, X. Phonon heat transfer across a vacuum through quantum fluctuations. *Nature* **2019**, *576* (7786), 243−247.

(3) Shen, S.; Narayanaswamy, A.; Chen, G. Surface phonon polaritons mediated energy transfer between nanoscale gaps. *Nano Lett.* **2009**, *9* (8), 2909−2913.

(4) Kim, K.; Song, B.; Fernandez-Hurtado, V.; Lee, W.; Jeong, W.; Cui, L.; Thompson, D.; Feist, J.; Reid, M. T.; Garcia-Vidal, F. J.; Cuevas, J. C.; Meyhofer, E.; Reddy, P. Radiative heat transfer in the extreme near field. *Nature* **2015**, *528* (7582), 387−391.

(5) Shi, K.; Sun, Y.; Chen, Z.; He, N.; Bao, F.; Evans, J.; He, S. Colossal Enhancement of Near-Field Thermal Radiation Across Hundreds of Nanometers between Millimeter-Scale Plates through Surface Plasmon and Phonon Polaritons Coupling. *Nano Lett.* **2019**, *19* (11), 8082−8088.

(6) Shi, K.; Chen, Z.; Xu, X.; Evans, J.; He, S. Optimized colossal near-field thermal radiation enabled by manipulating coupled plasmon polariton geometry. *Adv. Mater.* **2021**, *33* (52), 2106097.

(7) Salihoglu, H.; Nam, W.; Traverso, L.; Segovia, M.; Venuthurumilli, P. K.; Liu, W.; Wei, Y.; Li, W.; Xu, X. Near-Field Thermal Radiation between Two Plates with Sub-10 nm Vacuum Separation. *Nano Lett.* **2020**, *20* (8), 6091−6096.

(8) Fiorino, A.; Thompson, D.; Zhu, L.; Song, B.; Reddy, P.; Meyhofer, E. Giant Enhancement in Radiative Heat Transfer in Sub-30 nm Gaps of Plane Parallel Surfaces. *Nano Lett.* **2018**, *18* (6), 3711−3715.

(9) Du, W.; Yang, J.; Zhang, S.; Iqbal, N.; Dang, Y. D.; Xu, J. B.; Ma, Y. G. Super-Planckian near-field heat transfer between hyperbolic metamaterials. *Nano Energy* **2020**, *78*, 105264.

(10) DeSutter, J.; Tang, L.; Francoeur, M. A near-field radiative heat transfer device. *Nat. Nanotechnol.* **2019**, *14* (8), 751−755.

(11) Lim, M.; Song, J.; Lee, S. S.; Lee, B. J. Tailoring near-field thermal radiation between metallo-dielectric multilayers using coupled surface plasmon polaritons. *Nat. Commun.* **2018**, *9* (1), 4302.

(12) Yang, J.; Du, W.; Su, Y.; Fu, Y.; Gong, S.; He, S.; Ma, Y. Observing of the super-Planckian near-field thermal radiation between graphene sheets. *Nat. Commun.* **2018**, *9* (1), 4033.

(13) Song, B.; Thompson, D.; Fiorino, A.; Ganjeh, Y.; Reddy, P.; Meyhofer, E. Radiative heat conductances between dielectric and metallic parallel plates with nanoscale gaps. *Nat. Nanotechnol.* **2016**, *11* (6), 509−514.

(14) St-Gelais, R.; Zhu, L.; Fan, S.; Lipson, M. Near-field radiative heat transfer between parallel structures in the deep subwavelength regime. *Nat. Nanotechnol.* **2016**, *11* (6), 515−519.

(15) Shi, K.; Bao, F.; He, S. Spectral Control of Near-Field Thermal Radiation With Periodic Cross Resonance Metasurfaces. *IEEE J. Quantum Electron.* **2018**, *54* (1), 1−7.

(16) Zhou, C.-L.; Wu, X.-H.; Zhang, Y.; Yi, H.-L. Super-planckian thermal radiation in borophene sheets. *Int. J. Heat Mass Transfer* **2022**, *183*, 122140.

(17) Ito, K.; Nishikawa, K.; Miura, A.; Toshiyoshi, H.; Iizuka, H. Dynamic Modulation of Radiative Heat Transfer beyond the Blackbody Limit. *Nano Lett.* **2017**, *17* (7), 4347−4353.

(18) Ben-Abdallah, P.; Biehs, S. A. Near-field thermal transistor. *Phys. Rev. Lett.* **2014**, *112* (4), 044301.

(19) Fiorino, A.; Thompson, D.; Zhu, L.; Mittapally, R.; Biehs, S. A.; Bezencenet, O.; El-Bondry, N.; Bansropun, S.; Ben-Abdallah, P.; Meyhofer, E.; Reddy, P. A Thermal Diode Based on Nanoscale Thermal Radiation. *ACS Nano* **2018**, *12* (6), 5774−5779.

(20) Ito, K.; Nishikawa, K.; Iizuka, H.; Toshiyoshi, H. Experimental investigation of radiative thermal rectifier using vanadium dioxide. *Appl. Phys. Lett.* **2014**, *105* (25), 253503.

(21) Thomas, N. H.; Sherrott, M. C.; Broulliet, J.; Atwater, H. A.; Minnich, A. J. Electronic Modulation of Near-Field Radiative Transfer in Graphene Field Effect Heterostructures. *Nano Lett.* **2019**, *19* (6), 3898−3904.

(22) Ilic, O.; Thomas, N. H.; Christensen, T.; Sherrott, M. C.; Soljacic, M.; Minnich, A. J.; Miller, O. D.; Atwater, H. A. Active Radiative Thermal Switching with Graphene Plasmon Resonators. *ACS Nano* **2018**, *12* (3), 2474−2481.

(23) Zhou, C.-L.; Qu, L.; Zhang, Y.; Yi, H.-L. Enhancement and active mediation of near-field radiative heat transfer through multiple nonreciprocal graphene surface plasmons. *Phys. Rev. B* **2020**, *102* (24), 245421.

(24) Chen, G.; Jiang, L.; Wu, S.; Lyu, B.; Li, H.; Chittari, B. L.; Watanabe, K.; Taniguchi, T.; Shi, Z.; Jung, J.; Zhang, Y.; Wang, F. Evidence of a gate-tunable Mott insulator in a trilayer graphene moiré superlattice. *Nat. Phys.* **2019**, *15* (3), 237−241.

(25) Zhao, W.; Li, H.; Xiao, X.; Jiang, Y.; Watanabe, K.; Taniguchi, T.; Zettl, A.; Wang, F. Nanoimaging of Low-Loss Plasmonic Waveguide Modes in a Graphene Nanoribbon. *Nano Lett.* **2021**, *21* (7), 3106−3111.

(26) Zhao, W.; Zhao, S.; Li, H.; Wang, S.; Wang, S.; Utama, M. I. B.; Kahn, S.; Jiang, Y.; Xiao, X.; Yoo, S.; Watanabe, K.; Taniguchi, T.; Zettl, A.; Wang, F. Efficient Fizeau drag from Dirac electrons in monolayer graphene. *Nature* **2021**, *594* (7864), 517−521.

(27) Ott, A.; Hu, Y.; Wu, X.-H.; Biehs, S.-A. Radiative Thermal Switch Exploiting Hyperbolic Surface Phonon Polaritons. *Phys. Rev. Appl.* **2021**, *15* (6), 064073.

(28) Thompson, D.; Zhu, L.; Meyhofer, E.; Reddy, P. Nanoscale radiative thermal switching via multi-body effects. *Nat. Nanotechnol.* **2020**, *15* (2), 99−104.

(29) Shi, K.; Bao, F.; He, S. Enhanced Near-Field Thermal Radiation Based on Multilayer Graphene-hBN Heterostructures. *ACS Photonics* **2017**, *4* (4), 971−978.

(30) Zhao, B.; Guizal, B.; Zhang, Z. M.; Fan, S.; Antezza, M. Near-field heat transfer between graphene/hBN multilayers. *Phys. Rev. B* **2017**, *95* (24), 245437.
(31) Shi, K.; Liao, R.; Cao, G.; Bao, F.; He, S. Enhancing thermal radiation by graphene-assisted hBN/SiO2 hybrid structures at the nanoscale. *Opt. Express* **2018**, *26* (10), A591−A601.
(32) Liu, X. L.; Zhang, R. Z.; Zhang, Z. M. Near-field radiative heat transfer with doped-silicon nanostructured metamaterials. *Int. J. Heat Mass Transfer* **2014**, *73*, 389−398.
(33) Bernardi, M. P.; Milovich, D.; Francoeur, M. Radiative heat transfer exceeding the blackbody limit between macroscale planar surfaces separated by a nanosize vacuum gap. *Nat. Commun.* **2016**, *7*, 12900.
(34) Messina, R.; Ben-Abdallah, P. Graphene-based photovoltaic cells for near-field thermal energy conversion. *Sci. Rep.* **2013**, *3*, 1383.
(35) Falkovsky, L. A.; Pershoguba, S. S. Optical far-infrared properties of a graphene monolayer and multilayer. *Phys. Rev. B* **2007**, *76* (15), 153410.
(36) Bonaccorso, F.; Sun, Z.; Hasan, T.; Ferrari, A. C. Graphene photonics and optoelectronics. *Nat. Photonics* **2010**, *4* (9), 611−622.
(37) Shi, K. Z.; Bao, F. L.; He, N.; He, S. L. Near-field heat transfer between graphene-Si grating heterostructures with multiple magnetic-polaritons coupling. *Int. J. Heat Mass Transfer* **2019**, *134*, 1119−1126.
(38) Ghanekar, A.; Ricci, M.; Tian, Y.; Gregory, O.; Zheng, Y. Dynamic optical response of SU-8 upon UV treatment. *Opt. Mater. Express* **2018**, *8* (7), 2017−2025.
(39) Palik, E. D. *Handbook of Optical Constants of Solids*; Academic Press: San Diego, CA, 1985.
(40) Pisana, S.; Lazzeri, M.; Casiraghi, C.; Novoselov, K. S.; Geim, A. K.; Ferrari, A. C.; Mauri, F. Breakdown of the adiabatic Born-Oppenheimer approximation in graphene. *Nat. Mater.* **2007**, *6* (3), 198−201.
(41) Novoselov, K. S.; Geim, A. K.; Morozov, S. V.; Jiang, D.; Katsnelson, M. I.; Grigorieva, I. V.; Dubonos, S. V.; Firsov, A. A. Two-dimensional gas of massless Dirac fermions in graphene. *Nature* **2005**, *438* (7065), 197−200.
(42) Fei, Z.; Andreev, G. O.; Bao, W.; Zhang, L. M.; McLeod, A. S.; Wang, C.; Stewart, M. K.; Zhao, Z.; Dominguez, G.; Thiemens, M.; Fogler, M. M.; Tauber, M. J.; Castro-Neto, A. H.; Lau, C. N.; Keilmann, F.; Basov, D. N. Infrared nanoscopy of dirac plasmons at the graphene-SiO2 interface. *Nano Lett.* **2011**, *11* (11), 4701−4705.
(43) Fei, Z.; Rodin, A. S.; Andreev, G. O.; Bao, W.; McLeod, A. S.; Wagner, M.; Zhang, L. M.; Zhao, Z.; Thiemens, M.; Dominguez, G.; Fogler, M. M.; Castro Neto, A. H.; Lau, C. N.; Keilmann, F.; Basov, D. N. Gate-tuning of graphene plasmons revealed by infrared nano-imaging. *Nature* **2012**, *487* (7405), 82−85.
(44) Chen, J.; Badioli, M.; Alonso-Gonzalez, P.; Thongrattanasiri, S.; Huth, F.; Osmond, J.; Spasenovic, M.; Centeno, A.; Pesquera, A.; Godignon, P.; Elorza, A. Z.; Camara, N.; Garcia de Abajo, F. J.; Hillenbrand, R.; Koppens, F. H. Optical nano-imaging of gate-tunable graphene plasmons. *Nature* **2012**, *487* (7405), 77−81.

https://doi.org/10.1021/acs.nanolett.2c01286
Nano Lett. 2022, 22, 7753−7760